Heimly, Simen

Tropospheric measurements using the ALOMAR RMR-lidar

Temperature measurements using rotational raman spectrum and determination of the optical overlap.

Master's thesis

NTNU
Norwegian University of
Science and Technology

Preface

This thesis was written the last year of two year master physics program study at NTNU, Trondheim. The cases were proposed by Michael Gausa at Andøya Space Center, ASC, and was written in collaboration with them. The system used is owned by Leibniz-Instituts für Atmosphärenphysik in Kühlingsborn. I would like to thank my supervisor dr. Michael Gausa and ASC for the opportunity to work with them, the guidance and the opportunity to work at Andøya. I would also like to thank my supervisor prof. Patrick Espy at NTNU for guidance through the ending of the work, and dr. Gerd Baumgarten at IAP for all the insight and help with the thesis. Last I would also like to thank my girlfriend Aurora Haraldsen for all the support.

Abstract

The ALOMAR tropospheric lidar was not operative as the laser was damaged and could not be repaired. It got a new laser during the writing of this thesis. In this thesis I will try to give a backup solution using the RMR-lidar for tropospheric measurements, which is also located at ALOMAR. The RMR-lidar is equipped with rotational Raman channels which will be used to calculate the temperature. As the RMR-lidar is built for upper atmospheric measurements the telescopes have an incomplete optical overlap in the troposphere. The optical overlap function for the RMR telescopes will be determined using different methods, such that the RMR-lidar can be used for other measurements in the troposphere. The overlap function will then briefly be used to compare data from tropospheric lidar.

Contents

List of Abbreviations

ALOMAR Arctic Lidar Observatory of Middle Atmosphere Research

FOV   Field of view

GC   Geometrical compression

IAP   Leibniz-Institut für Atmosphären Physik

Lidar   Light Detection and Ranging

NA   Numerical aperture

NILU   Norsk intitutt for luftforskning

O(R)   Overlap function

PMT   Photomultiplier tube

RMR   Rayleigh-Mie-Raman

RR   Rotational Raman

CHAPTER 1

Introduction

Atmospheric lidar technology can be applied in many different studies. Lidar is an instrument sending laser pulses and measures the backscattered signal in different altitudes. The backscattered signal contains information about different parameters of the backscattering medium. It can be used for particle extinction studies [1], determining particle size [2], temperature measurements [3] just to name a few. Atmospheric research is critical to study and understand weather and climate. The use of remote sensing has become a convenient way to study the basic variables of state in the atmosphere such as temperature, pressure, humidity, and aerosols. Lidar systems gives an insight of the atmospheres properties at high spatial and temporal resolution for long periods of time.

The tropospheric lidar at the ALOMAR observatory is out of service because of a laser malfunction, determining an overlap function for the Rayleigh-Mie-Raman (RMR) can give some data in the period the tropospheric lidar is out of service. The tropospheric lidar uses elastic backscattering to calculate properties of the troposphere, and the RMR lidar uses the same wavelength laser and detection channels. But to use the RMR lidar for the same calculations the overlap function must be determined. The optical overlap function for the lidar system

will also be calculated using an approximated analytical solution, a numerical ray tracing simulation and an experimental approach. I will also attempt to measure the temperature in the troposphere using rotational Raman scattering theory as another solution. The RMR lidar is equipped with rotational Raman channels which uses the inelastic scattering of molecules to calculate the temperature.

CHAPTER 2

Lidar background theory

A lidar system consists of a transmitter and a receiver. The transmitter is a laser that shoots short pulses, typically the pulses are in the order of ns, and this determines the maximum resolution for the system. The detectors resolved time interval is Δt and determines the spatial resolution. Each resolution step is commonly called a range bin. The length of each range bin can be calculated by $\Delta R = c\Delta t/2$, where c is the speed of light. This is only valid if the laser pulse is shorter than the detector time. The factor $1/2$ is from the fact that the light has to move both ways in the range bin.

Lidar detection system consist of using photonmultiplier tubes, PMTs, to detect the backscattered photons in each range bin. The backscattered photons comes from either molecules or aerosols in the atmosphere giving information about the properties of the scattering medium.

2.1 The lidar equation

The lidar equation in its absolutely simplest form is

$$P(R) = KG(R)\beta(R)T(R), \tag{2.1}$$

where P is the received power, K is a constant which describes the total efficiency of the system, $G(R)$ describes how the intensity varies due to the geometry of the system. $\beta(R)$ and $T(R)$ are atmospheric variables, the backscatter and transmission coefficients respectively.

All of these terms can further be deconstructed. The total system factor K can be described as

$$K = P_0 \frac{c\tau}{2} A \cdot \eta, \tag{2.2}$$

where P_0 is the average power of a single laser shot, and τ is the temporal pulse length. These multiplied is equal to the energy of a single shot. A is the area of the receiver, and η the overall efficiency of only the detector system. The factor 1/2 comes from a folding of the laser as it travels trough the medium observed. G(R) is the geometrical decompression of the system, which is explained in the next subsection.

$\beta(R)$ is the backscatter coefficient determined by the backscattering medium. This is highly dependent on the wavelength of the laser,

$$\beta(R, \lambda) = \sum_j N_j(R) \frac{d\sigma}{d\Omega}(\pi, \lambda). \tag{2.3}$$

In eq 2.3 the backscatter is defined as the sum of all different backscatter elements j, with an abundance N, multiplied with the differential cross section $\frac{d\sigma}{d\Omega}$ in the backwards direction π. This is called the backscatter cross section. In the atmosphere there are two different contributors to backscattering, molecules which the air consists of, and aerosols (particulate matter). The backscatter can be decomposed into the two main different scattering mediums, molecular scattering and aerosol backscatter,

$$\beta(R, \lambda) = \beta_{mol}(R, \lambda) + \beta_{aer}(R, \lambda). \tag{2.4}$$

The molecular backscatter is primarily dependent on the abundance of O_2 and N_2. That means for ground based systems the backscatter decreases with range. The aerosol backscatter is highly variable in the atmosphere both spatial and temporal. There are many different particles that contribute to particle backscatter; sea-salt, dust, water droplets, soot, just to name a few. T is the transmission of the light in the atmosphere i.e. which percentage of the photons which is in the path to and from scattering medium. Here T(R) is defined as

$$T(R, \lambda) = \exp\left(-2\int_0^R \alpha(r, \lambda)dr\right), \tag{2.5}$$

where α is the sum of all the light extinction coefficients in the path.

K and G is determined by the systems specifications, while β and T are atmospheric variables to be determined [4].

For the transmission to be determined one needs to know the extinction coefficient. The most common method is called the Klett method, which was derived by James Klett in 1982 [5]. To solve the lidar equation one introduce a helping quantity

$$S(R) = ln[r^2 P(R)], \tag{2.6}$$

and using the assumption that the backscatter and extinction is related in a power law form

$$\beta = const \cdot \alpha^k, \tag{2.7}$$

where k is dependent on the lidar wavelength and the scattering medium, following ref [5] one end up with the far range solution,

$$\alpha(R, \lambda) = \frac{exp[S - S_m/k]}{\alpha(R_m, \lambda)^{-1} + \frac{2}{k}\int_r^{r_m} exp[(S - S_m)/k]dr'}. \tag{2.8}$$

It is called the far range solution as one choose a far distance R_m as reference to integrate to from a distance r. Instead of integrating from a distance to r.

2.2   The lidar profile

The lidar profile is the signal frequency received plotted against the altitude. The most common way to plot the lidar profile is the altitude on the y-axis and the logarithm of the photon count frequency on the x-axis. The photons received from scattering in clean air comes primarily from Rayleigh scattering of the air molecules. The signal goes down with altitude due to less Rayleigh scattering in a less dense atmosphere. It is expected by atmospheric conditions to decrease exponentially, which will affect the lidar profile. This is why the lidar profiles are often plotted with semi-logarithmic axes. With intensity on the x-axis and altitude on the y-axis. If we have perfect clean air, neglect extinction and geometrical compression the signal should only decrease due to lower pressure. The result would be a straight line in the semi-log plot.

Geometrically the signal decreases due to the telescopes overlap function and that the solid angle which spans the telescope area seen from the scattering medium decreases. Due to the solid angle decreasing the received signal is expected to decrease by a factor $\sim 1/R^2$ with altitude.
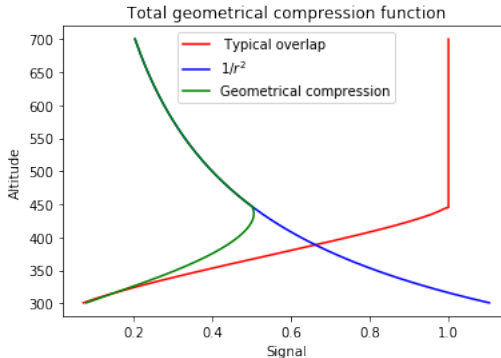
$$G(R) = O(R)/R^2 \tag{2.9}$$

Figure 2.1: The geometrical impact on the lidar signal. The blue line is due too the solid angle which spans the telescope area decreases with $1/r^2$, and the red line is due to an incomplete overlap of the laser beam and telescope FOV.

Here is a typical range-corrected lidar signal profile with an unknown overlap.
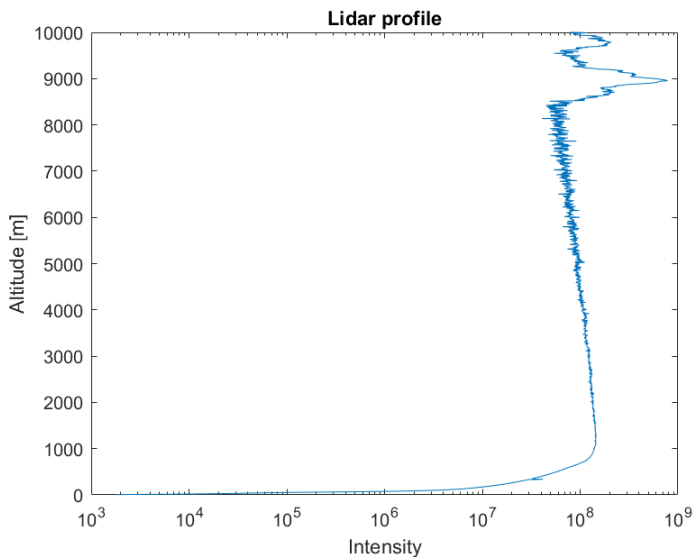

Figure 2.2: Range corrected lidar profile. One can see an incomplete overlap up too one kilometre, at five kilometres the signal starts to become noisy due to low counts at these altitudes. One can also note a cirrus cloud at 8-10 kms. Data: ALOMAR, 08.11.2018.

The geometrical parts of the received lidar signal are often taken care of by data processing, if the overlap function is determined. The necessary data processing of the raw signal will be described in the next chapter.

CHAPTER 3

Method

In this chapter I will go trough the equipment used for the RMR-lidar at ALOMAR, and the necessary raw data processing needed to make the lidar return usable for remote sensing.

3.1 Equipment

The Arctic Lidar Observatory for Middle Atmospheric Research, ALO-MAR, on Andøya is situated 69°N and 16°E. The observatory is equipped with an RMR twin lidar capable of temperature measurements, wind measurements, and measuring shape and size of particles in the atmosphere [6]. In the cited article there is an extensive description of the system, in this thesis I will only go through the most necessary parts. A general illustration of an atmospheric lidar in figure 3.1.
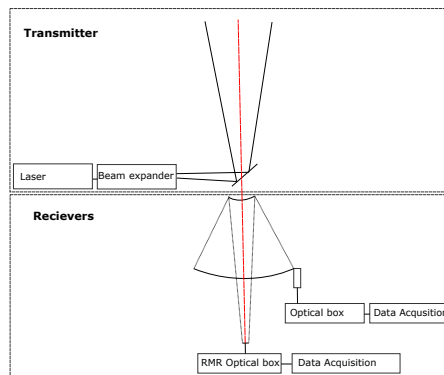
Figure 3.1: A lidar setup consisting of a transmitter part, a laser a beam-expander and a beam-guiding mirror, and a reciving part, a Cassegrain telescope with an optical box and data acquisition hardware. In addition to this there is a small lens telescope which is further mentioned in appendix A.

3.1.1 Setup

The RMR lidar consist of:

- Nd:YAG: Laser

- Cassegrain telescope

- Detector system

NdYag: Laser

The Nd:YAG emits an electromagnetic wave with the wavelength 1064 nm. By generation of optical harmonics in a crystalline quartz, we double and triple the frequency such that we receive two additional wavelengths, 532nm and 355nm [7]. The laser has a bandwith < 70 Mhz.The laser pulses have an energy of 360mJ and a frequency of 100 Hz. The laser is also externally seeded to make sure that the laser wavelength is stable. To keep the laser divergence low the laser goes through a beam expander such that the exit diameter of the laser is

20cm. The laser divergence δ is measured to be 35µrads after the beam expander. The actively stabilised to fit the optical axis at all time with an offset less than $\pm 20\mu$ rads.

Cassegrain telescope

The RMR receiver is a Cassegrain telescope with a diameter of 1.8 meters. The telescopes specifics are explained in more detail in chapter 5.2. A picture of the telescope at ALOMAR is given in figure 3.2.

Figure 3.2: The cassegrain telescope for IAPs RMR-Lidar situated at ALOMAR.

Detector system

To analyse the received signal we need as previously mentioned several channels of wavelengths counted. For the RMR system the received light signal goes from the telescope to the optical table via fiber.
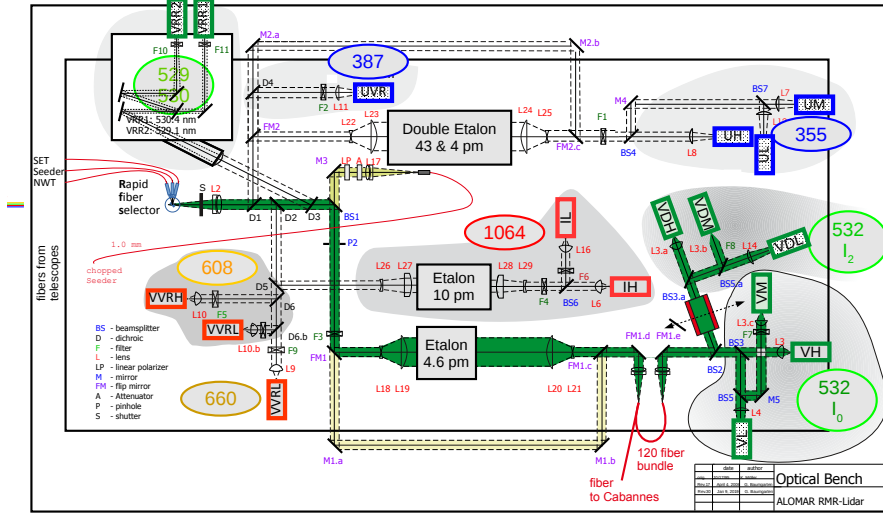

Figure 3.3: The optical table for the RMR lidar. Here the received light is filtered into wavelengths using dichroic filters and etalons. Courtesy of dr. Gerd Baumgarten.

The rotational Raman spectrum is challenging to filter out due to its closeness to the 532 nm Cabannes line received from elastic scattering which usually is a magnitude of order 3 or higher than the Raman spectrum.

The rotational Raman channels were verified to be in this spectrum. Using Perkin Elmer Lambda 900 spectrometer a high resolution scan over the optical system for the RR channels was performed. Guiding the light from the spectrometer through the optical bench to the RMR data acquisition system one can measure the spectral efficiency of the system. The scan went from 534 to 527 nm. The data interval was

0.01 nm with 10 seconds detector time for each data interval. This gives a scan time of 0.06 nm per minute which is used to convert the time axis of the data acquisition to wavelength. The slit of the spectrometer was 0.1 nm which is sufficient to measure the spectre of the r Raman channels. The results are plotted into the spectrum of O_2 and N_2 in figure 3.4.
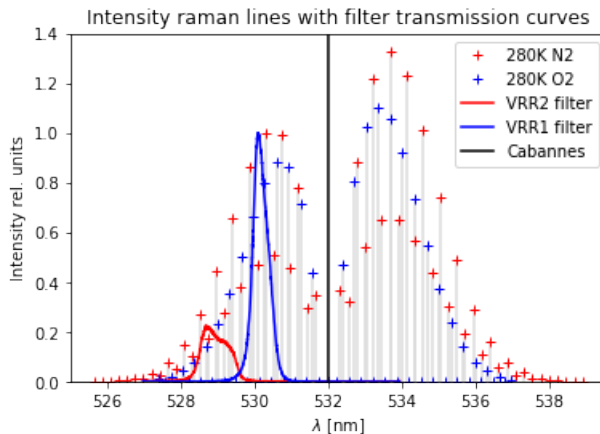

Figure 3.4: The efficiency of the detector channels was normalised to the peak of the VRR1 channel. The spectrum was normalised to the maximum intensity of the anti-stokes branch for N_2.

3.2 Data processing

The received raw lidar data has to be processed before use. When a laser pulse is shot into the atmosphere there is also a photo detector, also called a trigger, for the photon counter such that we can know where the laser pulse is. When light is scattered from the air or aerosols in the atmosphere some of it is then received by the LIDAR telescope.

At ALOMAR we use Licel transient recorders. The raw data is processed in 6 steps before we can further analyse it.

1. Dead-time correction.

2. Background subtraction.

3. Correction for zero-bin.

4. Range corrected signal(RCS).

5. Time correction between discrete photon-counting and analog signal.

6. Gluing of PC and analog signal.

1: The Licel photon counter have certain limitations when it comes to photon counting. Dead-time is the time where two separate photons can hit the photon counter and be counted as individual photons. This must be taken into account for low height measurement since the amount of photons scattered from the laser is high, which increases the likelihood of missing photons. This is a statistical problem which can be described as a non-paralyzable system [8]. In a non-paralyzable detector, an event happening during the dead time is simply lost. This means with increasing amount of events the detector will reach a saturation equal to the inverse of the dead time .Then the observed count rate can be given as:

$$N = \frac{S}{1 + S \cdot \tau_d} \tag{3.1}$$

Where N is the observed count rate, S is the true count rate and τ_d is the dead-time of the system. This can be inverted as:

$$S = \frac{N}{1 - N \cdot \tau_d} \tag{3.2}$$

This is a theoretical statistical model and can only be used if $N < \tau_d$. This means that this will be a good correction is good if the observed amount of photons per dead time is less than one on average.

2: There is also background scattered in the atmosphere, with the earth and sun as light sources. This background radiation have to be taken into account before we can further process the raw data. This is subtracted from the counted amount of photons. When the raw data is received, the observed counting rate becomes close to constant for

great heights or in between shots, the average of this is subtracted from all bins.

3: Then we need to correct for the zero-bin, this is a correction done to make sure that the first bin is the first altitude measured.

4: Now the signal can be range corrected. We approximate the scattering from air to be on average isotropic. This means that the solid angle of scattered light from a molecule which hits the telescope is decreasing with height. In fact it is decreasing to the factor $\frac{1}{R^2}$.

5: Photomultipliers used often have a possibility to measure a wide range of light intensities using two different modes, discrete photon counting and analog mode. For high intensity light the analog signal from the photonmultiplier is used, and the signal is the mean of the current observed. For low intensity light the current pulses can be counted individually for discrete counting. These two modes can be used at the same time and needs to be time corrected such that we ensure they are measuring at the same altitudes.

6: The two modes can then be glued together for a complete lidar profile.

During all these steps the measurement uncertainty are considered and combined using the standard Gaussian error propagation.

CHAPTER 4

Lidar temperature calculations using rotational Raman scattering

In this chapter i will briefly go through the history of Raman scattering and when it started to be used for remote sensing. Then go through the Raman theory needed to use it for temperature measurements and how it is implemented in lidar systems. I will introduce two techniques, one involving a reference measurement to calibrate to, and direct calculation using only the systems specifics.

4.1 Raman scattering

Raman scattering is inelastic scattering of light on molecules. This causes an energy interaction that changes the energy i.e. the frequency of the light. Raman scattering was first proposed by Adolf Smekal in 1923 [9]. In 1928 the Raman effect was discovered by C.V. Raman and his coworker K.S Krishnan by looking at a strong beam sunlight scattered through quartz [10]. Later Krishnan showed that the Raman spectrum was dependent on the current states of the scattering molecules i.e. the temperature of the medium [11]. The use of rotational Raman spectrum of backscattered light from the air was

first proposed by Cooney in 1971 [12]. He used the Raman rotational spectrum of N_2 to calculate the temperature in the atmosphere. Since then we have gotten more sophisticated laser and telescope setups for the lidar measurements.

4.1.1 Raman theory

Raman lidars use the weak inelastic scattering of light from atmospheric molecules. Inelastic scattering exchanges energy between the photon and the molecule. This changes the quantum state of the molecule and the frequency of the photon. If the molecule absorbs energy from the photon the photons frequency $\widetilde{\nu}$ decreases by $\Delta\widetilde{\nu}$. If the photon is red-shifted, the process is called Stokes Raman scattering [13]. If the molecule transfer energy to the photon the photon is blue-shifted, and is called anti-Stokes Raman scattering. The frequency shift

$$\Delta\widetilde{\nu} = \widetilde{\nu}_1 - \widetilde{\nu}_s = \frac{\Delta E}{c_0 \cdot h} \qquad (4.1)$$

is determined by the scattering molecule. ΔE is the energy difference between the molecular energy levels involved, and h and c_0 are the physical constants Planck's constant and the speed of light in vacuum respectively. In spectroscopy the common way to denote frequency is the wave number $\widetilde{\nu} = 1/\lambda$.

For homonuclear diatomic molecules such as O_2 and N_2 the energy levels can be well approximated by a freely rotating harmonic oscillator. The vibrational energy levels are given by:

$$E_{vib,\nu} = hc_0\widetilde{\nu}(v + 1/2), \qquad\qquad v = 0, 1, 2... \quad (4.2)$$

where v is the vibrational quantum number and $\widetilde{\nu}$ is the specific oscillator frequency.

The rotational energy levels are given to a good approximation

$$E_{rot,J,\nu} = hc_0[B_\nu J(J+1) - D_\nu J^2(J+1)^2], \qquad J = 0, 1, 2... \quad (4.3)$$

where J is the rotational quantum number. B_ν is a rotational constant and D_ν is the centrifugal distortion of the molecule. These constants

depend on the vibrational state ν of the molecule. For atmospheric conditions most of the molecules are in the ground vibrational state.

To receive the frequency shift we use the sum of the equations 4.2 and 4.3 to find a certain vibration-rotation energy level, and then apply this to equation 4.1. We consider the energy transition allowed by the quantum mechanical selection rules described in ref [13],

$$\begin{aligned}
\Delta v &= 0, \pm 1 \\
\Delta J &= 0, \pm 2.
\end{aligned} \tag{4.4}$$

One can in short term say that the intensity of a rotational Raman scattering line is

$$I_{J \to J'} = PNLF_J \cdot d\sigma_{J \to J'}/d\omega, \tag{4.5}$$

where P is the power of the incident beam, N is the number density of molecules, L is the length sample, F_J is the fraction of molecules in the state J. Last $d\sigma_{J \to J'}/d\Omega$ is the differential cross section.

The received Raman signal for a lidar setup depends on the differential cross section $d\sigma(\pi)/d\Omega$. This is also called the backscatter cross section. This cross section can be calculated from Placzek's polerizability [14] theory under the following assumptions:

1. The frequency of the incoming light is much larger than the possible vibration-rotation transition of the scattering molecule.

2. The frequency is much smaller than any electron transition frequency of the scattering molecule.

3. The ground state of the molecule is not degenerate.

For atmospheric conditions these assumptions have been shown to hold [4].

The absolute Raman scattering cross section under these conditions

has been shown to be for incident light with frequency ν_0, [15]

$$\left(\frac{d\sigma}{d\Omega}\right)_\pi^{RR,i} = \frac{112\pi^4}{15} \cdot \frac{g_i(J)hcB_{0,i}(\nu_0 + \Delta\nu_i(J))^4\gamma_i^2}{(2I_i + 1)^2 kT} \cdot X(J) \cdot$$
$$\exp(\frac{-E_{rot,i}(J)}{kT}).$$

(4.6)

Here the Placzek-Teller coefficients are in $X(J)$ term and found in
ref [16]. For the Stokes branch

$$X(J) = \frac{(J+1)(J+2)}{2J+3}, \qquad for \qquad J = 0, 1, 2, ...$$

(4.7)

and for the anti-Stokes branch

$$X(J) = \frac{J(J-1)}{2J-1}. \qquad for \qquad J = 2, 3, 4, ...$$

(4.8)

$g_i(J)$ is the statistical weight factor dependent on the nuclear spin I_i. k
is Boltzmann constant, T is the temperature, and γ_i is the anisotropy
of the polerizability tensor of the molecule i. The statistical weight
factors are

	$g_i(J)$	
	J odd	J even
N_2	3	6
O_2	0	1

Table 4.1: The statistical weight factors for N_2 and O_2

From this one can calculated the number of photons received by the
system with

$$S_{RR}(z) = S_0\epsilon\frac{AO(z)}{z-z_0}\Delta z N(z)\left[\sum_{i=O_2,N_2}\sum_{J_i}\tau_{RR}(J_i)\eta_i\left(\frac{d\sigma}{d\Omega}\right)_\pi^{RR,i}(J_i)\right]\cdot$$
$$\tau_{atm}(z_0, z)^2$$

(4.9)

Where τ_{RR} is the systems efficiency at the frequency of the RR line
J_i. η_i is the relative volume abundance of the molecule.

The constants have been experimentally determined and are found in
table 4.2.

Molecular constants			
	$B_{0,i}$ cm^{-1}	$D_{0,i}$ cm^{-1}	γ_i^2 cm^6
N_2	1.98959 [17]	$5.76 \cdot 10^{-6}$ [17]	$0.51 \cdot 10^{-48}$ [18]
O_2	1.43768 [19]	$4.85 \cdot 10^{-6}$ [19]	$1.27 \cdot 10^{-48}$ [18]

Table 4.2: The ground state rotational $B_{0,i}$ and centrifugal distortion
constant $D_{0,i}$, and the squared anisotropy of the polarizability tensor.

Using this one can find the RR spectrum for N_2 and O_2. One have
to take into account the abundance of N_2 and O_2 which is 0.7808 and
0.2095 respectively.

The pure RR spectrum without Doppler and pressure broadening is
plotted in figure 4.1 and 4.2.
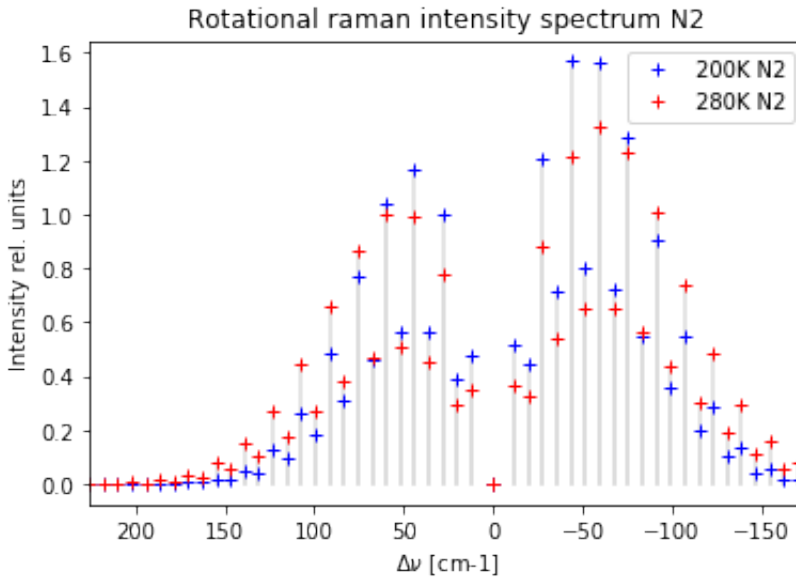
Figure 4.1: The nitrogen RR spectrum, the intensity has been nor-
malised to 1 for the strongest Anti-Stokes line at 280K. The incoming
wavelength is 532 nm.
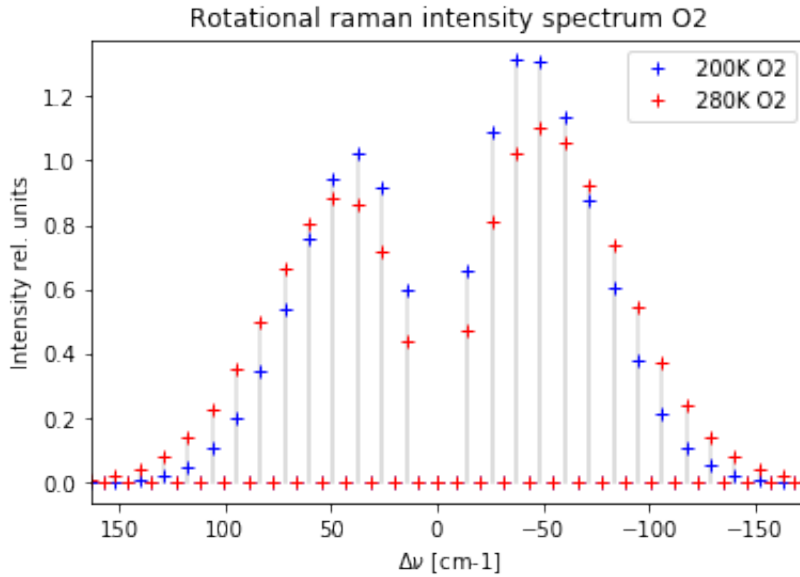
Figure 4.2: The oxygen RR spectrum, the intensity has been normalised to 1 for the strongest Anti-Stokes line at 280K for nitrogen. The incoming wavelength is 532 nm.

One can from figure 4.1 and 4.2 see that the spectrum is stronger near the incident wavelength for lower temperatures. While at higher rotational quantum numbers the signal is strongest for higher temperatures, as expected. Choosing two different RR-lines as channels in the detection, one decreasing with temperature and one increasing with temperature to calculate temperatures.
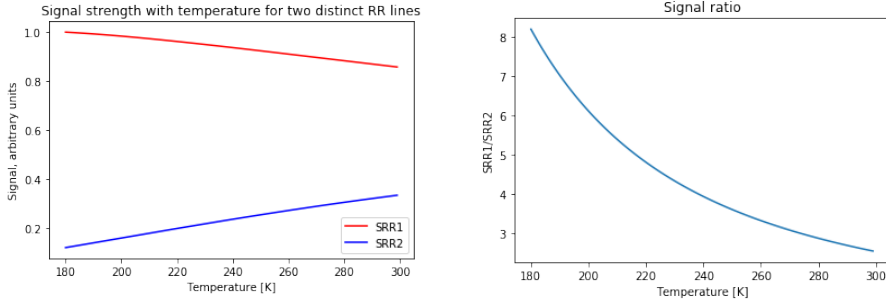
(a) The signal for two theoretical RR-channels with temperature.

(b) The signal ratio between two theoretical RR-lines.

Figure 4.3: Theoretical pure RR-lines.

This can in theory be used exactly if one knew the exact properties of the lidar system. One can also use models and fitting the signal ratios to temperatures measured by a radiosonde, which will be introduced in the next chapter.

4.1.2 Doppler broadening

Until now we have considered pure RR lines. As the molecules are moving there will be a Doppler broadening of the lines. This will have an impact on the signal ratios received by the lidar. The frequency shift can be written as:

$$f = f_0(1 + \frac{v}{c}) \tag{4.10}$$

The speed of the molecules is evenly distributed in a direction to and from the observer which will result in a broadning of the spectral line.

$$P_f(f)df = P_v(v_f)\frac{dv}{df}df \tag{4.11}$$

Inserting $v_f = c(\frac{f}{f_0} - 1)$:

$$P_f(f)df = \frac{c}{f_0} P_v(c(\frac{f}{f_0} - 1))df \qquad (4.12)$$

For thermal Doppler broadning the velocity distribution is given by
the Maxvell distribution.

$$P_v(v)dv = \sqrt{\frac{m}{2\pi kT}} exp\left(-\frac{-mv^2}{2kT}\right)dv \qquad (4.13)$$

Comparing these will give a Gaussian distribution with standard de-
viation:

$$\sigma_f = \sqrt{\frac{kT}{mc^2}} f_0 \qquad (4.14)$$

4.1.3 Temperature models using radiosonde data

One knows that the quantum states of the molecules in the air is
dependent on the temperature following the Boltzmann distribution.
The ratio between the different states and therefor the Raman signals
can then be used to calculate the temperature of the air. The RMR-
setup at the ALOMAR uses the rotational Raman spectrum at 530.4
nm and 529.1 nm. Both of these are Stokes lines and the reason this
is used is to avoid the fluorescence effect from N_2 [20]. The probability
of backscatter at 291.1 nm is increasing with increasing temperature
while at 530.4 it is decreasing.

The temperature at an altitude z can be calculated using [20]

$$T(z) = \frac{B}{A + \log(R(z))}, \qquad (4.15)$$

where $R(z)$ is the signal ratio between the two different rotational
Raman signals

$$R(z) = \frac{SRR1(z)}{SRR2(z)}. \qquad (4.16)$$

The two constants A and B has to be determined using radiosonde data. The temperature should be measured as close to the lidar setup as possible. These constants will fluctuate as the system is calibrated and should therefore be recalculated every once in a while to ensure a certain stability in the temperature measurements. The model above is exact for two pure Raman lines, using detector systems covering multiple Raman lines an even better approximation given by

$$T(z) = \frac{-2a'}{b' \pm \sqrt{b'^2 - 4a'(c' - \ln(R(z)))}}. \qquad (4.17)$$

This model have three calibration constants, a', b' and c' which needs to be determined.

4.2 Raman temperature results

The ALOAMR RMR lidar collects data from the rotational Raman spectrum of N_2 and O_2 centred at 530.4 nm and 529.1 nm [21]. These channels will be refereed to as RR1 and RR2. The 08.02.19 the weather conditions were good and air was quite clean except at 5km. These conditions are good to calibrate the model constants in eq 4.15 to the radiosonde data, this will also check if the Mie scattering processes is sufficiently suppressed in the Raman channels.
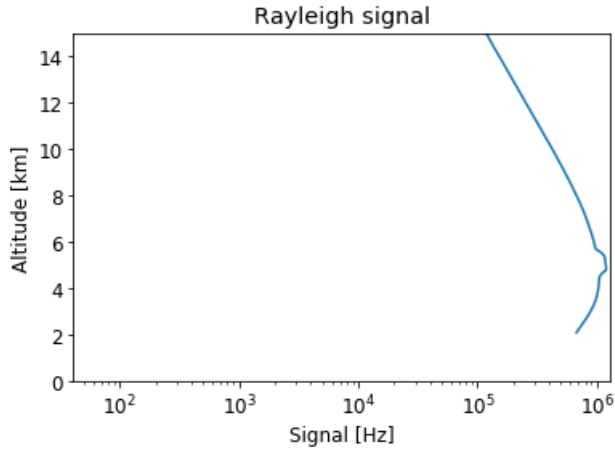
Figure 4.4: Signal at 532 channel with 1 hour of integration. Data:
08.02.19
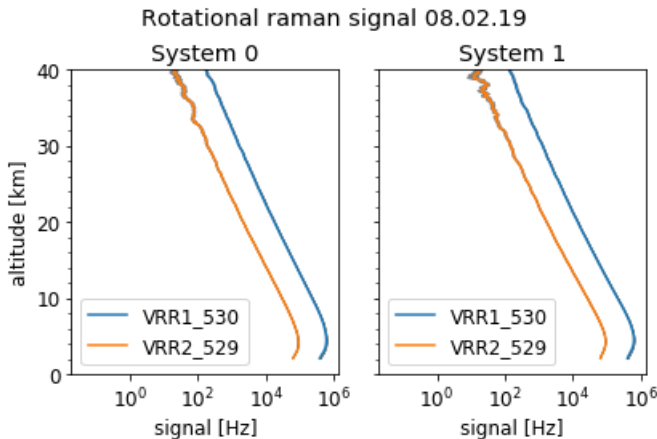
Figure 4.5: Rotational Raman signals with one hour of integration.
2019-02-08 23:00:00 UT, ALOMAR

One can see that the signal above 30km is too uncertain to be used as
one can see the grey error area, especially for high temporal resolution
temperature measurements. Which is fine because the area of interest
is the troposphere.

The radiosonde data was interpolated to the same altitude axis as
the lidar data. Then a least square fit was performed between the

measured radiosonde temperature and the signal ratio through the model in equation 4.15.

4.2.1 Model fit 1

The signal data was fitted to the temperature measurements from a radiosonde released within the hours of the lidar measurements. These were then fitted through the model in equation 4.15.
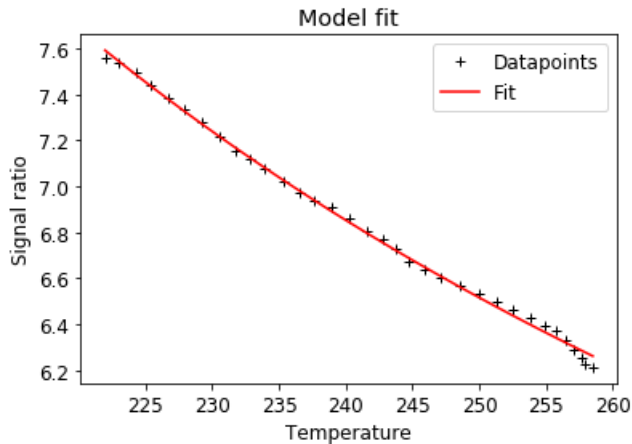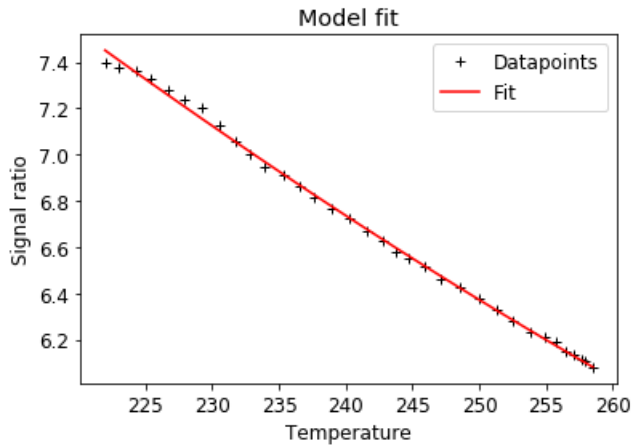

Figure 4.6: Model fit to determine the model constants, using data from fig 4.5. The datapoints are constructed using temperature from radiosonde data and signal ratio from the lidar at the same altitudes.

The constants were then used to calculate the temperature the following balloon release, 24 hours after the calibration measurements, to have a reference to check if the model is within error calculation ranges.
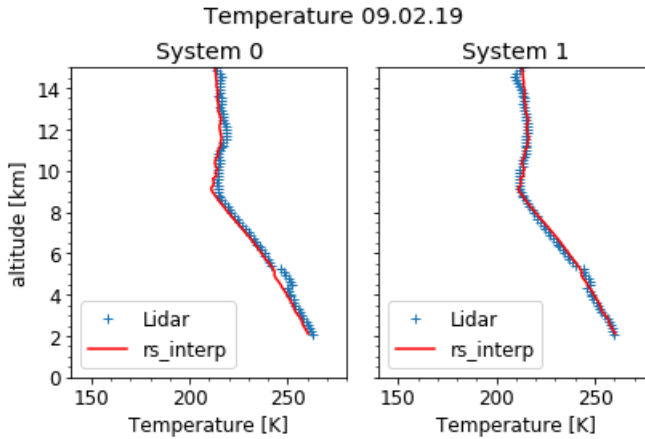
Figure 4.7: Temperature from interpolated radiosonde data and lidar
RR calculations with one hour integration. Radiosonde data: 2019-
02-08 23:05:00, ALOMAR. Lidar data in figure C.5.

Error calculations were performed as explained in appendix B, taking
measurement uncertainty and model fit errors into account.
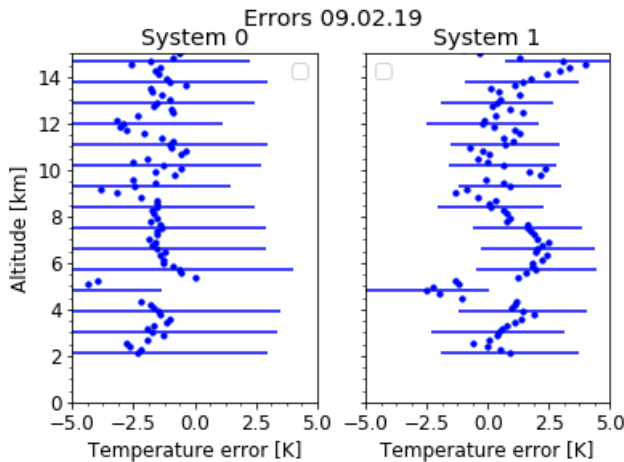
Figure 4.8: Errorbars of 1 σ plotted into the relative errors.

One can see that the relative error is within the measurement errors
expect at roughly 5 km. The 09.02.19 had a thin cloud layer one can
see from the data set used in figure C.5. This gives an indication

that the Cabannes line is not sufficiently suppressed for high accuracy temperature measurements.

4.2.2 Model fit 2

Performing the same routine as previously described with the second model equation 4.17.

Figure 4.9: Model fit to determine the model constants, using data from figure 4.5. The datapoints are constructed using temperature from radiosonde data and signal ratio from the lidar at the same altitudes. 2019-02-08 23:05:00, ALOMAR
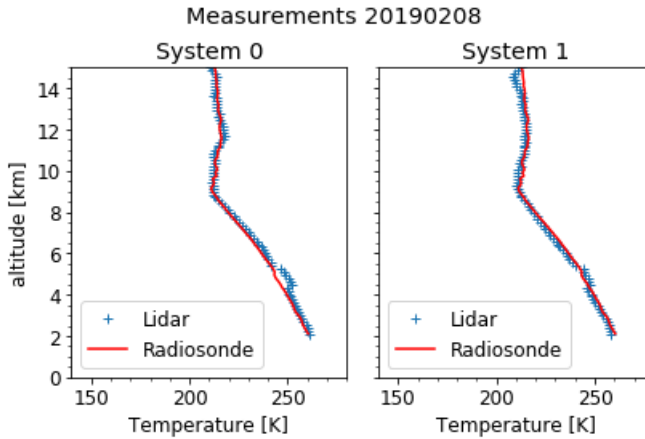
Figure 4.10: Temperature from interpolated radiosonde data and lidar
RR calculations with one hour integration.
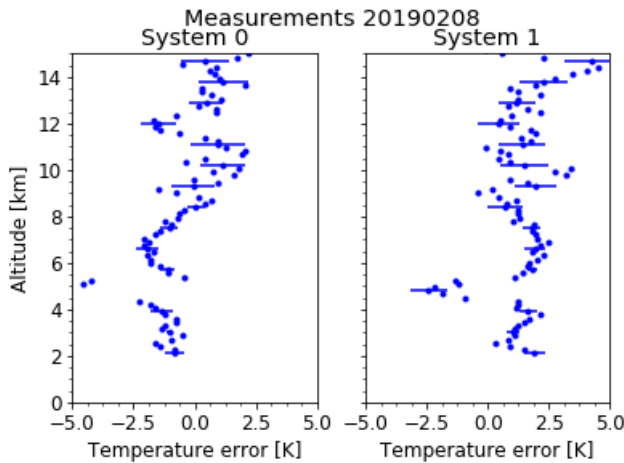
Figure 4.11: Errorbars of 1 σ plotted into the relative errors.

Here the uncertainty is well below 1K, but the correlation is very high
between the calibration constants. One can also see that the error is
higher than the uncertainty especially at 5 km confirming the before
mentioned suspicions of influence from the Cabannes line.

4.2.3 Errors

Since the correlation of the constants are so high for the second model, the focus was changed to improving the first model with two calibration constants. The idea is to find a condition such that if there is too much elastic backscatter it subtracts a small percentage of the Cabannes signal from the Raman channels. This will give a new signal ratio:

$$R(z) = \frac{SRR1(z) - c \cdot SVL(z)}{SRR2(z) - d \cdot SVL(z)} \qquad (4.18)$$

the constant c and d can then be fitted to a day with high elastic backscatter.
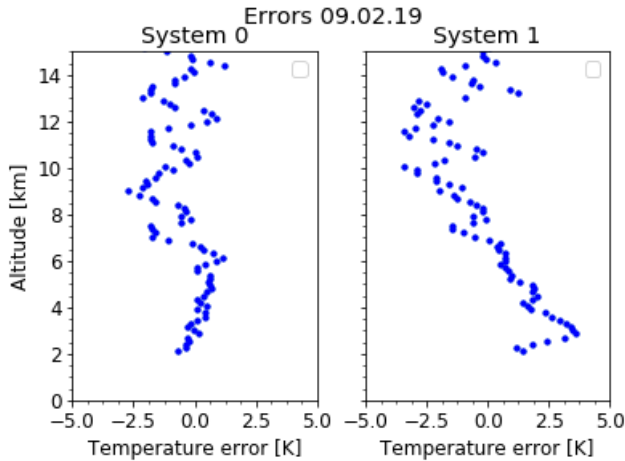
Figure 4.12: Error subtracting a small percentage of the Cabannes signal.

4.2.4 Stability of the calibration constants

To ensure that the model can be used in between the radiosondes we have to ensure that the calibration constants of the systems do not vary or drift dramatically. The constants can be calculated each

radiosonde release to evaluate if they are stable enough. Looking at
the results from data from 2018 and 2019 the constants fluctuates a
lot from month to month, although they seem stable enough to keep
the measured data within the uncertainty from day to day. One can
in figure 4.13 see some of the signal ratio to radiosonde temperature
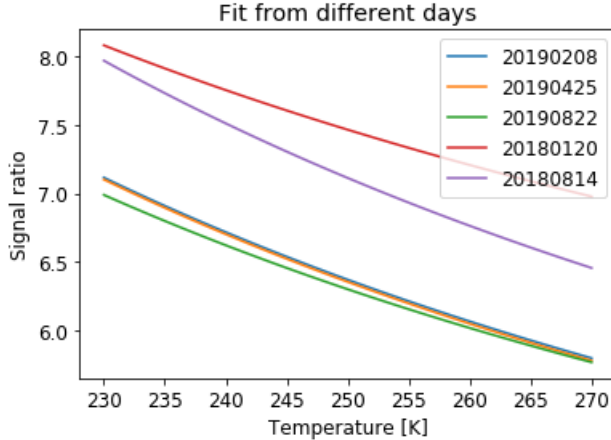fits performed from the data in 2018 and 2019.

Figure 4.13: Different signal ratio fits to radiosonde temperature data.
Here one can see that the data from 2019 are more stable than 2018.

4.2.5   Temporal resolution

The longer the measurement series the more data. The more data the
lower uncertainty. Assuming a perfect model and knowing the calibra-
tion constants for model 1 exactly the error has been calculated using
standard gaussian error propagation between the raman channels.

$$U(T) = \left(\frac{b}{SRR1(a - \log(Q)^2}\right)^2 \cdot U(SRR1)^2 + \\ \left(\frac{b}{SRR2(a - \log(Q)^2}\right)^2 \cdot U(SRR2)^2 \tag{4.19}$$

The uncertainty is calculated at 5km altitude and plotted against time
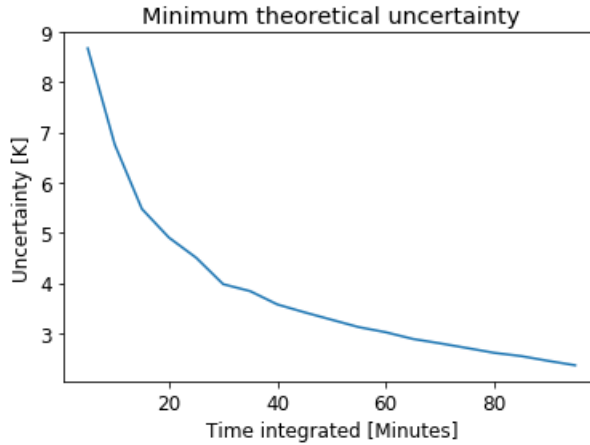integrated for an ideal condition in figure 4.14.

Figure 4.14: Theoretical minimum error, given a perfect model using
only signal uncertainties. Data used is plotted in figure C.1

4.2.6 Direct temperature calculations

One can use the information of the exact shape of the filters to calcu-
late the signal ratio directly from the spectrum. This is done by first
measuring the shapes of the filters, then multiplying the efficiency with
the Doppler broadened spectrum explained in chapter 4.1.1 and 4.1.2.
This can then be integrated for both channels to calculate the relative
intensities received from each channel. The brevity of this explanation
does not comprehend the computational challenges.
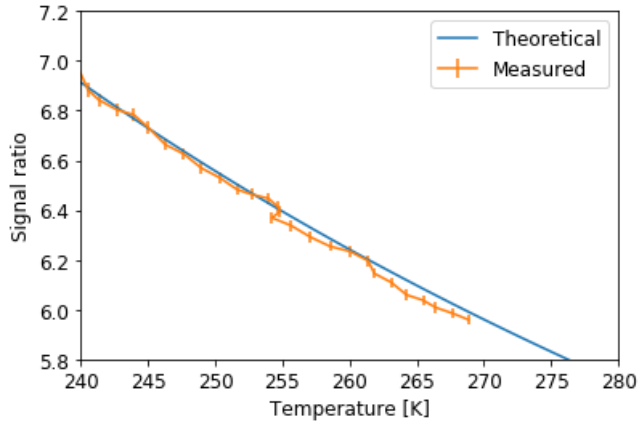
Figure 4.15: The signal ratio is theoretically computed from theory
and measured filter shapes. Radiosonde data, fig C.10. Lidar data
used from 22.08.19, 02:00:00 LT, ALOMAR, fig C.9

The data used is the closest to the measurements of the filters. Unfortunately the radiosonde release is 13 hours before the data was taken,
which is an unknown uncertainty. One can from figure C.10 see that
there is an unusual temperature inversion at 4 km which explains the
abnormality at signal ratio 6,4 in figure 4.15.

CHAPTER 5

Overlap problem

In this chapter I will first briefly describe the impact of the overlap function. Then I will describe the method of which I calculate the overlap function and the result of the method before moving on to the next method.

To be able to solve the lidar equation 2.1, one needs to know the total geometrical compression $G(R)$ of the system in equation 2.9. The range dependence is taken care of by data processing, but the compression due to incomplete optical overlap between the beam and the telescopes FOV is not always known. The equation given by

$$O(R) = \frac{E_{det}}{E_{telescope}},$$
(5.1)

computes the ratio of the light that hits the telescope that reach the detector. Assuming that the radiation hitting the telescope is isotropic we can write:

$$A_{eff} = O(R) \cdot A_i,$$
(5.2)

where A_{eff} is the effective area of the aperture, and A_i is the image

of the scattered laser light.

5.1 Stelmaszczyk, Overlap function

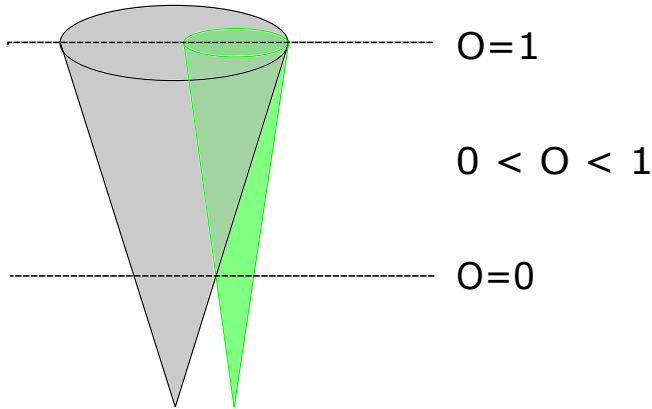Stelmaszczyk found a geometrical expression for the overlap of biaxial systems [22].

Figure 5.1: Illustration of the overlap area for biaxial lidar systems.

In this treatment we assume uniform laser intensity cross section and that the aperture is placed in the focal plane of the telescope.One can then calculate the area of the image of the laser as

$$e(R) = f\left(\delta + \frac{g_0 + T}{R}\right), \tag{5.3}$$

where f is the focal length, δ is the divergence of the laser, g_0 is the initial size of the beam, T is the telescope size, and R is the height. If one have a biaxial system the image will also get shifted, and one could also tilt the telescope towards the laser beam. To help us we introduce the new variable ν,

$$\nu(R) = f \cdot \frac{d_0 - \theta \cdot R}{R}. \tag{5.4}$$

Then we can calculate the overlap of these which is the area of the intersection of these circles. To calculate this we introduce the angles as in ref [22],

$$\psi_1(R) = \left(2 \cdot arccos\left[\frac{s^2 + 4\nu(R)^2 - e(R)^2}{4 \cdot \nu(R) \cdot s}\right]\right) \qquad (5.5)$$

$$\psi_2(R) = \left(2 \cdot arccos\left[\frac{e(R)^2 + 4\nu(R)^2 - s^2}{4 \cdot \nu(R) \cdot s}\right]\right). \qquad (5.6)$$

Then the overlap is

$$\xi(R) = \frac{[\psi_1(R) - sin(\psi_1(R)]s^2 + [\psi_2(R) - sin(\psi_2(R)]e(R)^2}{2\pi e(R)^2}] \qquad (5.7)$$

This is used for calculating an approximate overlap function for the experimental telescope in appendix A.

Coaxial system

For the coaxial system a much simpler method is used, with the same assumptions as earlier. Note that for the coaxial system the aperture is not in the focal plane.
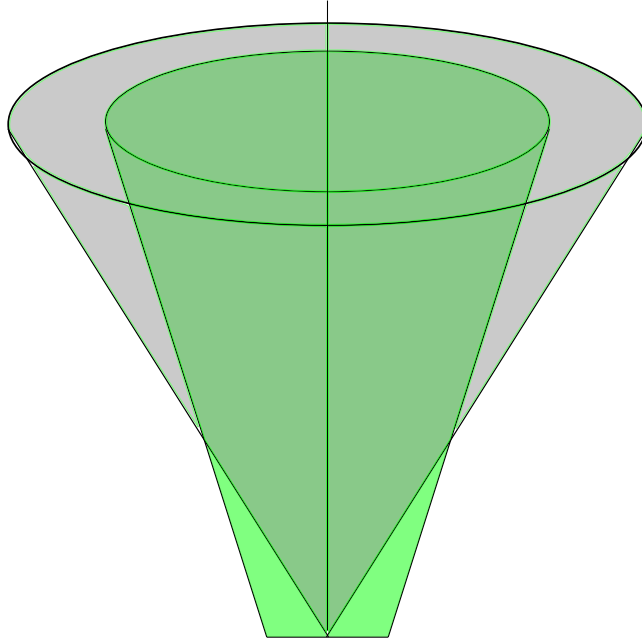
Figure 5.2: Illustration of the overlap area for coaxial lidar systems.

The vertical displacement of the image as the object moves towards the lens or mirror causes the image size to increase where the fiber is placed. Depending on where the fiber is placed one can achieve different and better overlap functions. This computation can simply be done by using equation 5.2. The only thing we now need is a term for the size of the laser image at the point where we put the fiber. We know that the distance to the image plane is

$$i = \frac{o \cdot f}{f - o}, \tag{5.8}$$

where o is the distance to the object and f is the focal length. We also know that the image size is

$$h_i = \frac{-h_o \cdot i}{o}, \tag{5.9}$$

where h_o is the size of the object, which in our case is the laser beam. The laser beam diverges ie. the object changes size and the image plane moves as the object plane moves. Since we for lidar system do

not care about the clarity of the image, we only care about the amount of the objects light which hits the fiber. This can be computed using trigonometry to be

$$y = \frac{T \cdot (i + x - f_0)}{i + x}, \tag{5.10}$$

where x is

$$x = \frac{h_i \cdot i}{T - h_i}, \tag{5.11}$$

where f_0 is the placement of the fiber and T is the radius of the telescope. Using this method the image obviously can be smaller than the fiber and therefore all values of the overlap function larger than one has to be discarded.

Aperture size :	0.0008 m
Focal Length :	8.345m
Laser divergence :	50 μ rads
Initial laser diameter :	0.2 m
Mirror diameter :	1,8 m

Table 5.1: Parameters for the big telescope

If the fiber was placed in the image plane one would quickly achieve full overlap. But this is not technically possible as the image plane changes with height. Another possibility is to place the fiber in the focal point of the telescope, the results of these hypothetical solutions are found in figure 5.3.
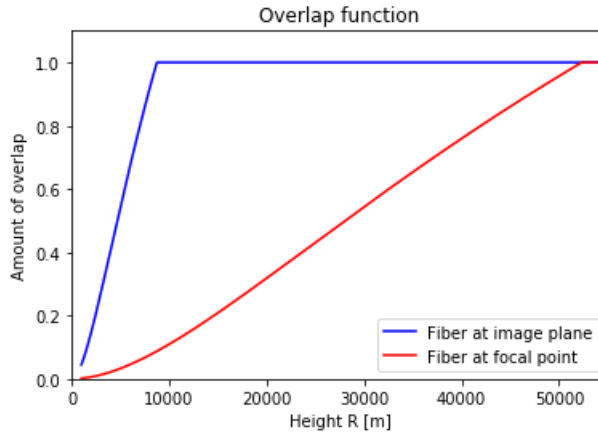
Figure 5.3: Overlap functions if the fiber is at the focal plane and if it could be in the image plane for all altitudes.

As we can observe this does not give overlap at an acceptable height. Therefore the fiber has been moved 2.7mm behind the focal point. The movement of aperture has a great impact on the overlap function as seen in figure 5.4.
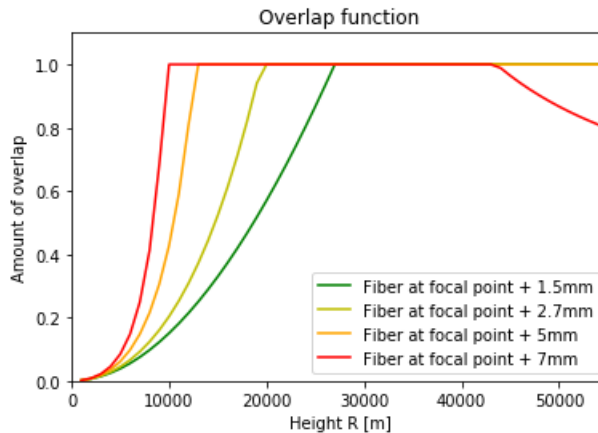

Figure 5.4: The overlap functions with different fiber positions.

5.2   Ray tracing simulations

The geometrical approach assumes geometrical optics, hence it omits spherical aberrations. In a spherical mirror with diameter 1.8 meters this is a huge error and need to be taken into account. The secondary mirror of the telescope has an aspherical shape to try and reduce the amount of spherical aberrations. Another assumption made is that the laser intensity is constant in the cross-section of the illuminated volume, while it's known that the laser beam has a Gaussian distribution.

The RMR telescopes are Cassegrain setups of one spherical primary mirror and one aspherical secondary mirror, as seen in figure 3.2.

Primary mirror	
Specifics	
Shape	Spherical
Curvature radius	5988 $\pm$ 1 mm
Diameter	1813.6 mm
Central hole	299.65 mm

The the shape of the secondary mirror is given by:

$$z = \frac{cr^2}{1 + \sqrt{1 - c^2 r^2}} + a_4 r^4 + a_6 r^6 + a_8 r^8 + a_{10} r^{10} \tag{5.12}$$

where $c = \frac{1}{R}$.

Secondary mirror	
Specifics	
Shape	Aspherical
R	-2878.088mm
c	-3.47453·10^{-4} mm^{-1}
Diameter	580 mm
a_4	-4.388·10^{-11} mm^{-3}
a_6	1.32·10^{-17} mm^{-5}
a_8	-2.0 ·10^{-23} mm^{-7}
a_{10}	-2.0 ·10^{-27} mm^{-9}
Mirror distance	2070 mm

Fiber	
Specifics	
R	0.75mm
Numerical aperture	0.11

Laser	
Specifics	
Initial radius	100 mm
Laser divergence	¡100 µrads

To compute the overlap function a Monte Carlo approach is used, follwing the steps:

- Calculate the size of the laser cross section given a laser divergence.
- Choosing a random initial position in the cross section, which is Gaussian distributed.
- Choose a random angle which hits the primary mirror.
- Run the ray tracing calculating intersections and mirroring angles to check if it hits the aperture fiber at a appropriate incident angle.

An appropriate angle is dependent on the numerical aperture of the fiber, NA which is a dimensionless number defined as

$$NA = n\sin(\theta), \tag{5.13}$$

where n is the refractive index of the fiber and θ is the incident angle.

To simplify the ray tracing we project the ray tracing to two dimensions. To compensate for this the angles are distributed circular such that more rays are hitting the edges of the telescope than the centre, as if it was a circle and not a line. Another big assumption made is that the intensity of the laser is constant with altitude, neglecting Rayleigh and Mie extinction.
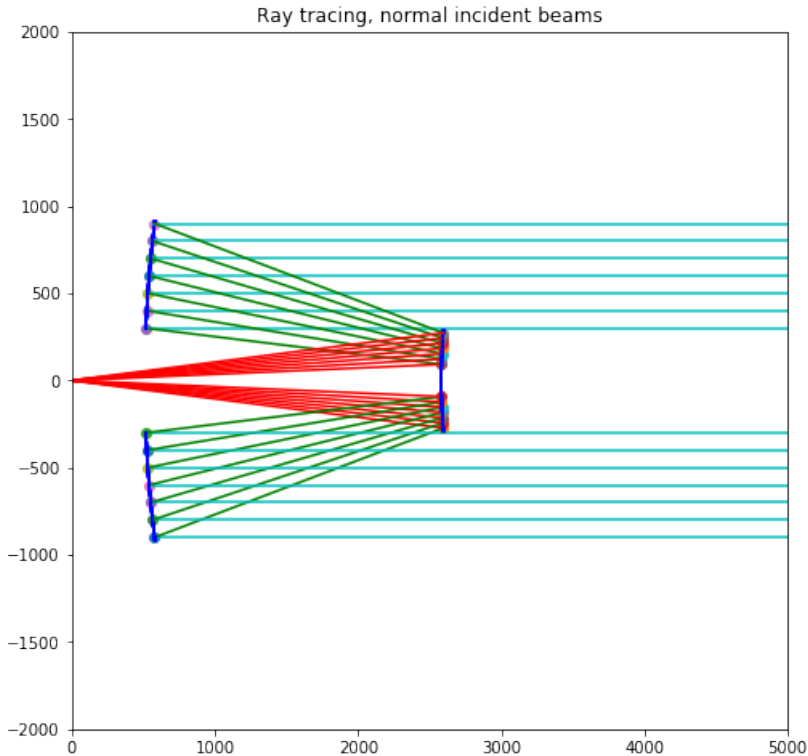
Figure 5.5: An illustration of the ray tracing performed with normal incident beams equally spaced.

All the Monte Carlo simulations were run with 100.000 randomly gen-

erated rays at each altitude. The altitude range was from 0.5-20km calculated at 60 steps.

First we run the simulation with and without the block of the secondary mirror to check if it gives an intuitive result.
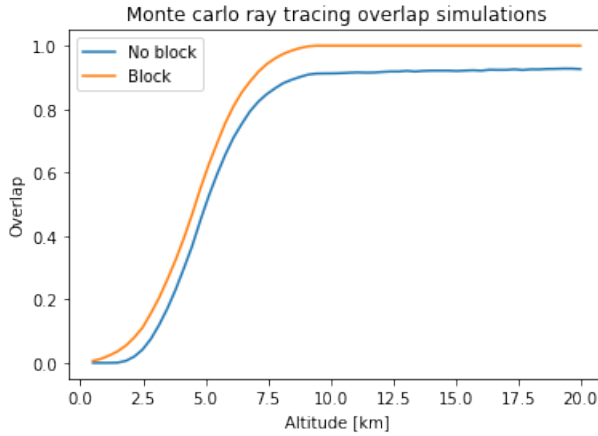
Figure 5.6: Overlap function with and without block.

One can see that the block has a greater impact on the overlap at lower altitudes as expected. The overlap only reaches approximatly 0.9 with the block because the block covers 10% of the primary mirror area.

The simulation was also run for different fiber positions and laser divergences which can be optimized after the results have been used to compare the data from the old tropspheric lidar and the corrected RMR-lidar.
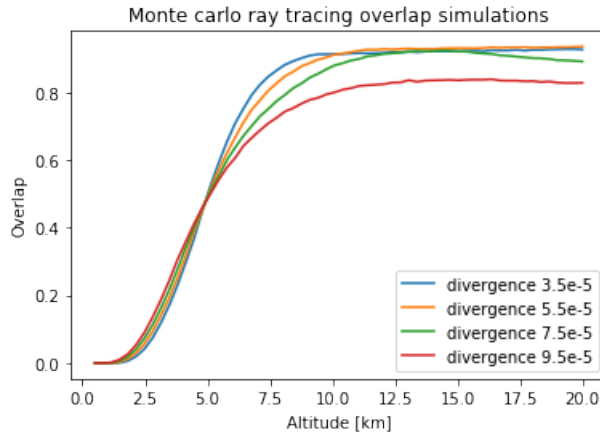
Figure 5.7: Overlap function with different laser divergences, focus is set at 507mm behind primary mirror.

One can see that the overlap is worse as the divergence of the laser increases as expected.
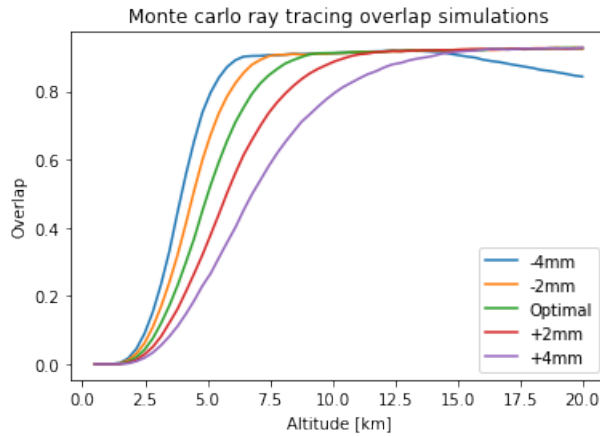
Figure 5.8: Overlap function with different focuses, laser divergence set to 35µrad

5.3   Experimental approach

The overlap can also be determined using the data received and using models for comparison [23]. For Raman signals the scattering medium is molecules only and therefore the backscatter coefficient β_R is only dependent on oxygen and nitrogen backscatter. The power received can be written as

$$P_R(z) = C_R O_R(z) z^{-2} \beta_R(z) T_0(z) T_R(z), \qquad (5.14)$$

where C_R is a system constant, O is the overlap function, T_0 is the transmission of the initial wavelength, and T_R of the Raman scattered wavelength. This can be re-written to

$$O_R(z) = \frac{P_R(z) z^2}{C_R \beta_R(z) T_0(z) T_R(z)}. \qquad (5.15)$$

We know that the Raman backscatter cross section is range independent, this means that the backscatter from equation 2.4 is only dependent on $N_j(R)$ i.e. the density. Correcting for the transmission of the initial wavelength for the path to the scattering medium and for the Raman scattered light for the path back to the receiver, one can find a C_R such that the $O(R)$ is 1 for full overlap range.

The transmission is found using Modtran [24]. Modtran is a moderate solution model for Lowtran 7 [25]. The software uses the 1976 U.S. Standard model to calculate the transmission of different wavelength light, prefect for this calculation. One can also set the path to be at an angle, and since the RMR-lidar often is tilted at 30 degrees this is necessary. The pressure is also simply calculated with models using the initial pressure at sea level.

Using data from the 20.01.02 the overlap was calculated and compared to one of the ray tracing simulations. The ray tracing overlap was redefined such that the maximum overlap is at 1 and not 0.9. They are then comparable as the experimental overlap naturally has maximum overlap including the block.
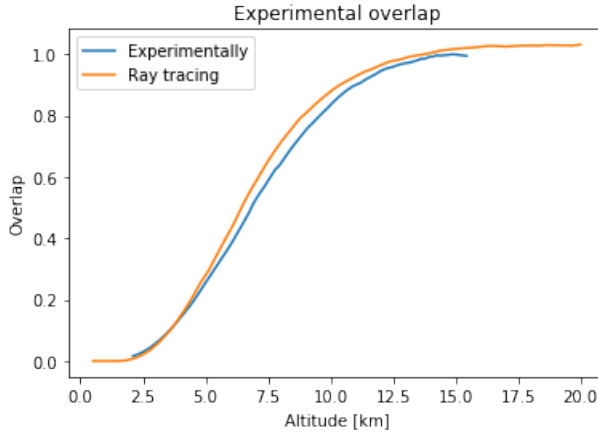
Figure 5.9: Experimentally determined overlap function, using 355 nm transmitted light and the received stokes vibrational Raman line of N_2 at 387nm.

5.4   Comments on the overlap function

Due to time restriction the results presented in this section will be brief. The overlap functions should be tested against the tropospheric lidar data available. The RMR lidar is often tilted to measure wind speeds at high altitudes using Doppler shift, and to be able to compare the two systems both should be measuring in zenith. Due to different formats of the data files finding data was tedious work, but should be continued.

The results presented is from one single measurement series and is used to give an idea of the overlap functions calculated. The geometrical overlap presented in figure 5.4 with the fiber placed at +2.7 nm was introduced to the RMR signal in figure C.12, the result is presented in figure 5.10.
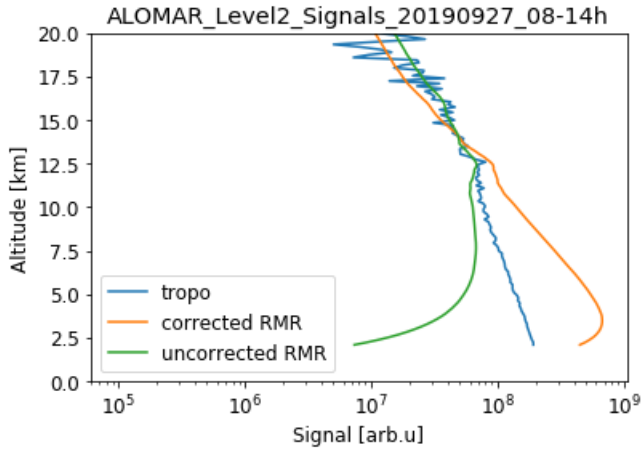
Figure 5.10: Comparison of the tropospheric lidar using the geometrical overlap function

From figure 5.10 one can see that the geometrical overlap approach was a bit naive and over corrects the signal. The geometrical approach does not give a good representation of the system. The same comparison is done using the overlap from the ray tracing simulation.
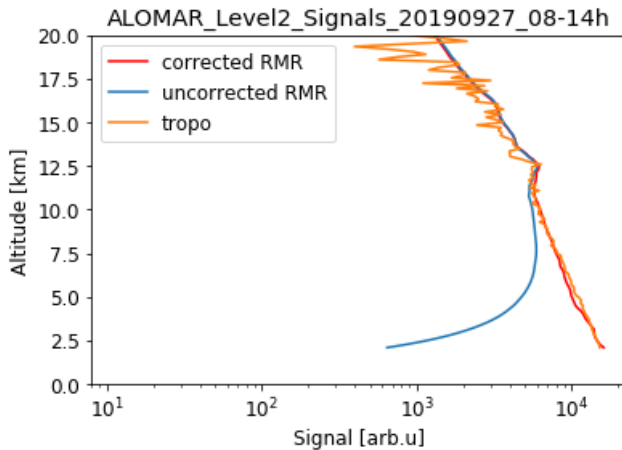

Figure 5.11: Comparison of the tropospheric lidar using the ray tracing simulated overlap function with laser divergence of 80 µ rads and a focus +1.75mm behind the optimal focus given by IAP.

From figure 5.11 one can see that the simulated overlap function is a much better method than the geometrical overlap. This is because this method gives a more accurate representation of the system. The slight errors might come from laser beam axis divergence and that the laser beam divergence itself is not constant.

CHAPTER 6

Conclusion and further work

Rotational Raman temperature measurements were done by using a model and direct calculations. It was found that the efficiency of the Raman channels was not sufficient for high temporal resolution measurements, but they are suitable for average temperatures in the upper troposphere. They may be used for seasonal temperature studies around the tropopause. The filter shapes can be used to directly measure the temperature, but are not needed as long as the model constants are calibrated each radiosonde release, and fortunately there is a NILU station close to ALOMAR which is scheduled to release balloons every 12th hour. It was also found that the RR channels are influenced by the Cabannes band and could be improved using more narrow filters. Further work includes fully automating the calibrations with suitable conditions for recalibrations, I would also recommend looking into possibilities of further suppressing the Cabannes band.

The overlap function is determined with three different approaches. The analytical geometrical approach does not give an accurate solution for the function. The ray tracing simulations neglect beam axis divergence and possible movements of the telescope due to temperature differences. The direct experimental approach has a resemblance to the ray tracing simulation but should be improved by using the it-

erative approach in ref. [23], instead of using models. The ray tracing overlap was unfortunately only tested using one single dataset, from figure 5.11 it seems to be quite accurate. The system is made for upper atmospheric atmospheric measurements, the beamguiding system that ensures stability of the measurements have a reference point above the atmosphere. Because of this the overlap function might not be stable and the solution given in figure 5.11 must be tested using more measurements. One could also test the solution for the extinction coefficient in equation 2.8

APPENDIX A

My little lidar

One of the methods explored to determine the overlap function was the use of a secondary smaller telescope to measure at the same time as the RMR lidar. Multiple problems were encountered, making this project just worthy of a mentioning in the appendix. First I can mention the advantages of this approach. This approach uses the same trigger and transmitter as from the RMR lidar, making the backscatter received from the scattering comparable. The secondary telescope had a much shorter focal length and approximately the same aperture size, this results in a much bigger field of view. The secondary telescope therefore gets a full overlap at significantly lower altitudes. The problems with the setup will be described next. Because of the large field of view the lens telescope was better suited for night time measurements. The setup was bi-axial making the setup extremely sensitive to any slight disturbances in the angle of the telescopes optical axis.

Figure A.1: The secondary telescope mounted to the side of the primary telescope.

The lenses tested were plano-convex lenses from Thorlabs, LA1238 and LA1353. Both with a diameter of 75 mm and with focal lengths 100mm and 200mm respectively. The overlap functions were calculated using equation 5.7, with the parameters in table A.1.

Aperture size :	0.0006 m
Focal Length :	100mm
Laser divergence :	70 μ rads
Initial laser diameter :	0.2 m
Lens diameter :	0.075 m
Initial distance :	1m

Table A.1: Parameters for the small telescope
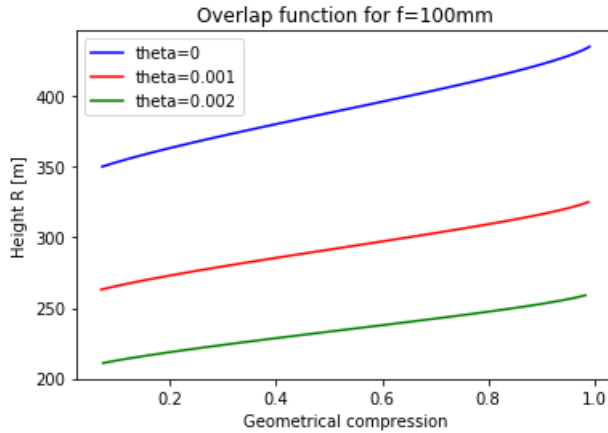
Figure A.2: Overlap function for different angles between the telescope optical axis and the lasers optical axis in radians.

One can see in figure A.2 that the sensitivity of where full overlap is achieved due to inclination differences. The telescope was mounted to the side of the RMR telescope, and had to be manually adjusted using an inclinometer. The inclinometer had an accuracy of 0.0005 degrees. The focus of telescope was also found manually using a camera pointing and pointing the telescope at distant mountains, which one in optics can call approximately infinity.

For a long time the data received didn't make sense, so I decided to mount a camera to the telescope to see what the field of view of the telescope looked like.
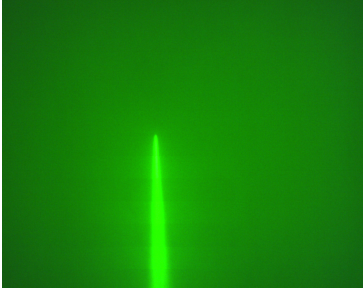
Figure A.3: Picture of the beam through the small telescope using a Thorlabs camera and green pass filter with no iris.
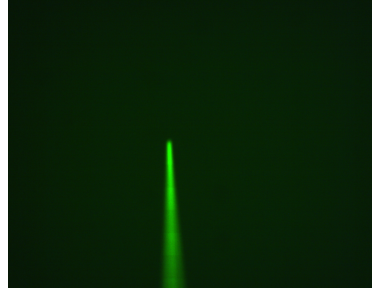
Figure A.4: Picture of the beam through the small telescope using a Thorlabs camera and green pass filter with 36mm diameter iris.

One can see that the spherical aberrations from the lens smeared the beam out over the camera chip. This means that light that should never hit the fiber does. The solution was to put on an iris to reduce the field of view and also the spherical aberrations is less close to the centre of the lens. This was at cost of the signal but the signal had to be suppressed using filters to not saturate the PMTs.

I could only receive one of the three wavelengths from the transmitter at once. The three channels were tested before I decided that the best signal was received at the 532 nm.

After this work the signal still got unexpected noise at random times. This error were never corrected and some measurement series were useless. To protect the equipment the measurements can only be done with wind under 12 m/s, no rain or snowfall and humidity below 90%. During my trip to Andøya in November I got the setup working, but during my stay in February I did not get an opportunity to measure due to weather conditions and laser maintenance work.

The few measurement series I got was also really inconsistent due to my work could not interfere with the RMR lidar measurements. The RMR lidar does wind measurements after 1 hour, which means that the telescopes tilts 30°of zenith. Because of the measurement range

of the inclinometer, and for safety reasons, I could not measure if the lens telescopes optical axis still was parallel to the laser beam making the measurements invalid.

One of the good measurements taken is given in figure 2.2. One can see that the estimation for where full overlap is achieved is roughly correct, but one receives signal where there should not be any. Therefore I will conclude that the overlap in equation 5.7 is not suitable for overlap calculations of this system. This means that if my little lidar can only be used for measurements above 1km.

APPENDIX B

Error calculations

Error propagation calculations were performed. After the calibration constants were fitted to the model using scipy optimizing packages the variance-covariance matrix was retrieved defined as:

$$K_{x_1,x_2,x_3} = \begin{bmatrix} \sigma_{x_1}^2 & \sigma_{x_1}\sigma_{x_2} & \sigma_{x_1}\sigma_{x_3} \\ \sigma_{x_1}\sigma_{x_2} & \sigma_{x_2}^2 & \sigma_{x_2}\sigma_{x_3} \\ \sigma_{x_1}\sigma_{x_3} & \sigma_{x_2}\sigma_{x_3} & \sigma_{x_3}^2 \end{bmatrix}. \tag{B.1}$$

Using Pearsons correlation coefficent,

$$\rho_{x_m,x_n} = \frac{cov(x_m, x_n)}{\sigma_{x_m}\sigma_{x_n}}. \tag{B.2}$$

One can calculate the propagation of uncertainty U for a function f

with correlated variables x_1, x_2, x_3 using

$$
\begin{aligned}
U(f)^2 = {}& \left(\frac{\partial f}{\partial x_1}\right)^2 U(x_1)^2 + \left(\frac{\partial f}{\partial x_2}\right)^2 U(x_2)^2 + \left(\frac{\partial f}{\partial x_3}\right)^2 U(x_3)^2 \\
& + 2\rho_{x_1,x_2}\left(\frac{\partial f}{\partial x_1}\right)\left(\frac{\partial f}{\partial x_2}\right)U(x_1)U(x_2) \\
& + 2\rho_{x_1,x_3}\left(\frac{\partial f}{\partial x_1}\right)\left(\frac{\partial f}{\partial x_3}\right)U(x_1)U(x_3) \\
& + 2\rho_{x_2,x_3}\left(\frac{\partial f}{\partial x_2}\right)\left(\frac{\partial f}{\partial x_3}\right)U(x_2)U(x_3)
\end{aligned}
\tag{B.3}
$$

APPENDIX C

Data

In this appendix I will add data I've used for the different calculations. This is to ensure a natural flow of the results. If nothing else is specified the data is from system 0 of the RMR-lidar. The radiosonde data is gathered from a Norwegian institute for air research, NILU, station just a couple of hundred meters from the ALOMAR observatory.
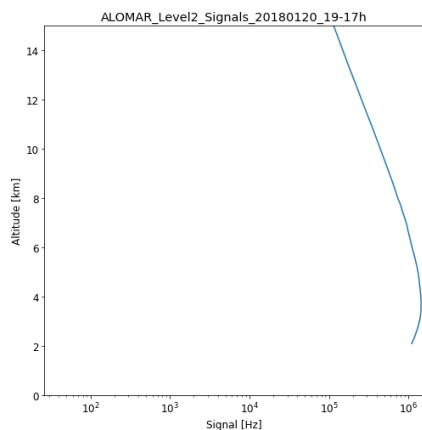
(a) 532 nm channel
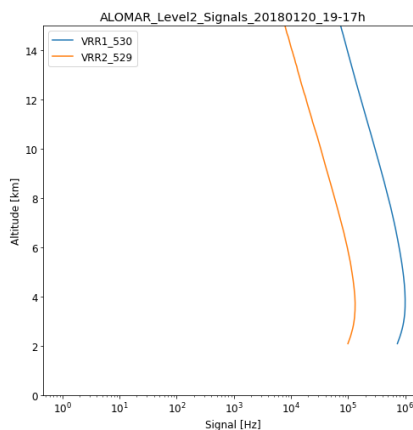
(b) Rotational raman channels
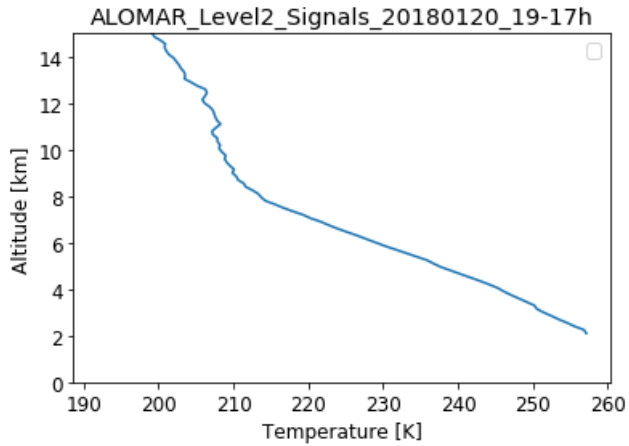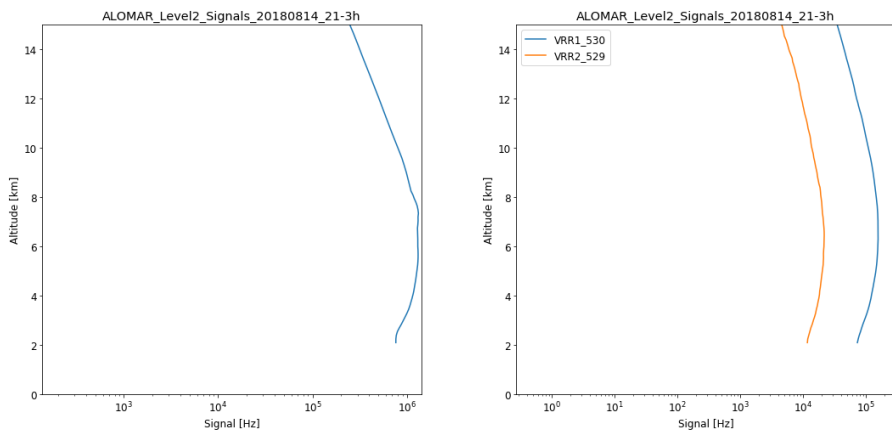
Figure C.1: 2018-01-20 23:00:00 UT, ALOMAR, integrated 1 hour.

Figure C.2: Interpolated radiosonde data, 2018-01-20 23:04:03 UT, ALOMAR

(a) 532 nm channel

(b) Rotational raman channels

Figure C.3: 2018-08-14 22:59:35 UT, ALOMAR, integrated 1 hour.
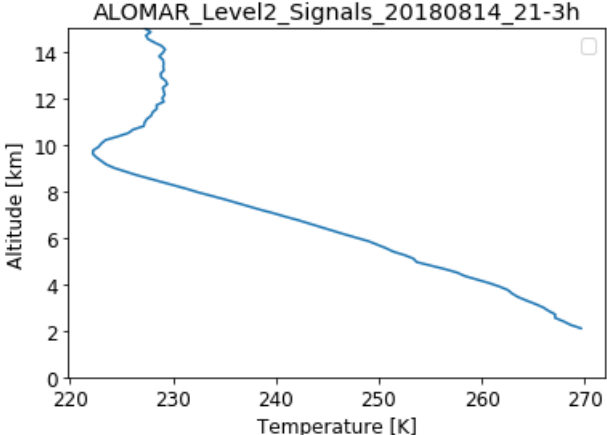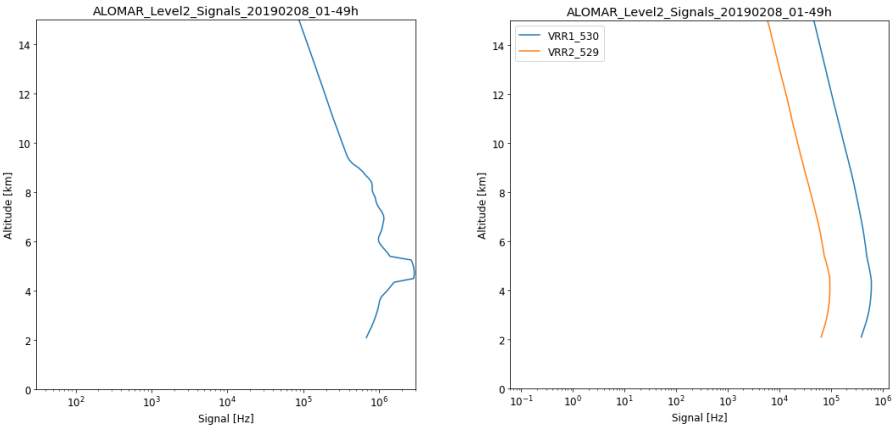
Figure C.4: Interpolated radiosonde data, 2018-08-14 17:03:00 UT, ALOMAR

(a) 532 nm channel

(b) Rotational raman channels

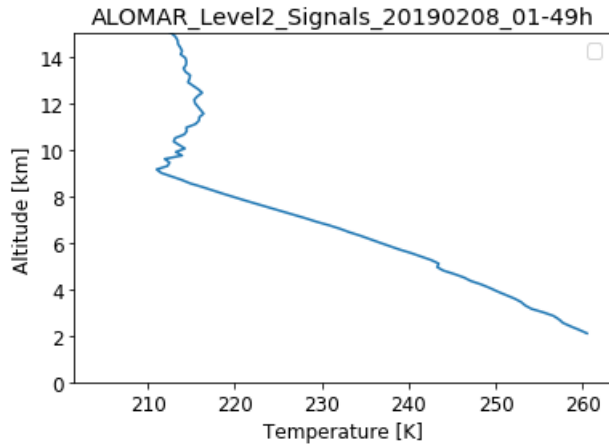Figure C.5: 2019-02-09 23:00:00 UT, ALOMAR, integrated 1 hour.
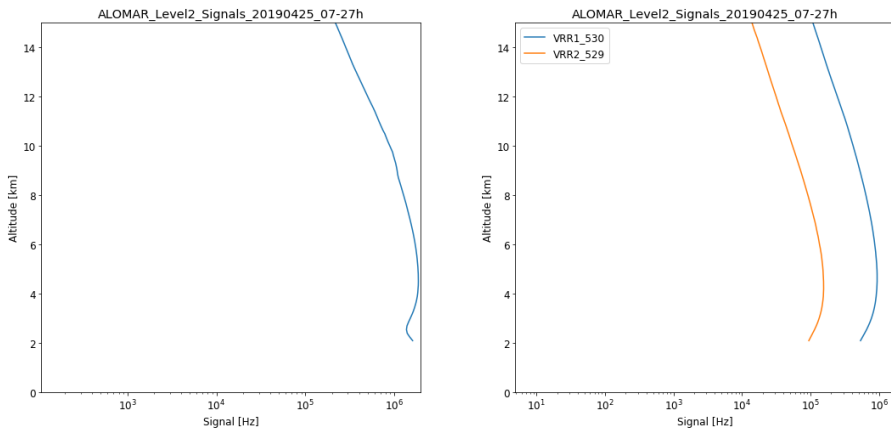
Figure C.6: Interpolated radiosonde data, 2019-02-09 23:06:00 UT, ALOMAR

(a) 532 nm channel

(b) Rotational raman channels

Figure C.7: 2019-04-25 23:00:00 UT, ALOMAR, integrated 1 hour.
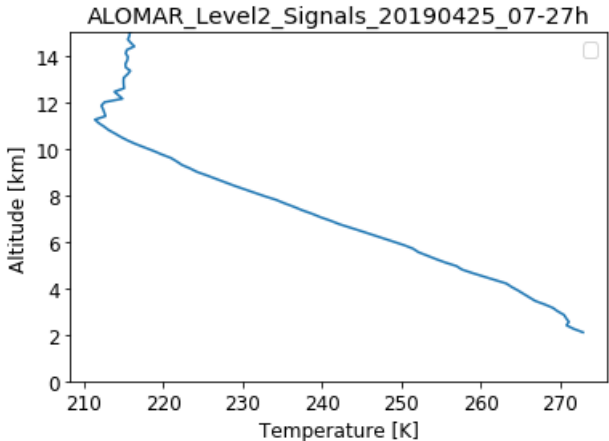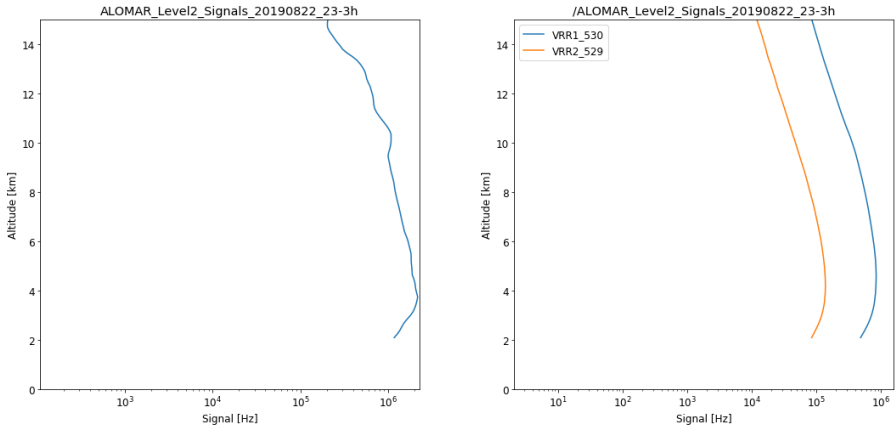
Figure C.8: Interpolated radiosonde data, 2019-04-25 23:06:00 UT, ALOMAR

(a) 532 nm channel

(b) Rotational raman channels

Figure C.9: 2019-08-23 00:00:00 UT, ALOMAR, integrated 1 hour. Data closest to the filter scan, one hour of integration.
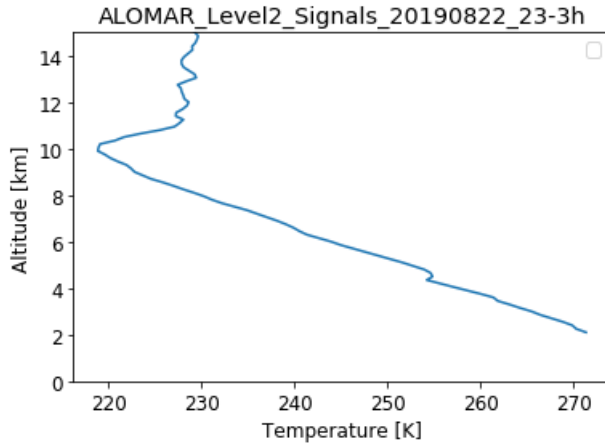
Figure C.10: Interpolated radiosonde data, 2019-08-22 11:11:00 UT, ALOMAR

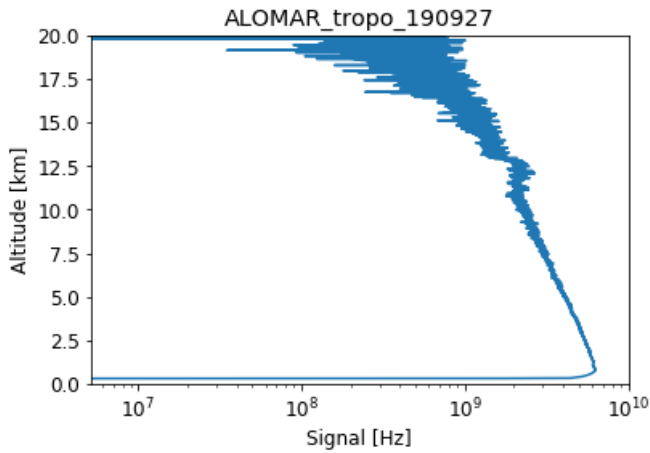Data for the tropospheric lidar comparison in figure C.11 and C.12.

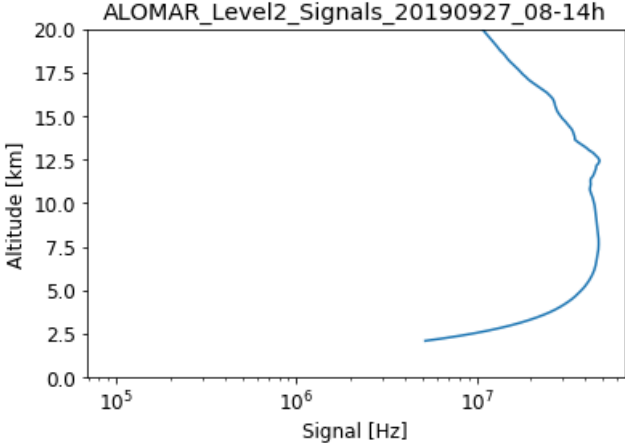Figure C.11: 532 nm channel 2019-09-27 10:00:19-12:07:37 UT

Figure C.12: 532 nm channel 2019-09-27 09:00:00-10:00:00

Bibliography

[1] David Whiteman. 1064 nm rotational raman lidar for particle extinction and lidar-ratio profiling: cirrus case study. *Atmospheric Measurement Techniques*, 9(9):4269–4278, 2016.

[2] G. Baumgarten, J. Fiedler, F.-J. Lübken, and G. von Cossart. Particle properties and water content of noctilucent clouds and their interannual variation. *Journal of Geophysical Research: Atmospheres*, 113(D6), 2008.

[3] S. M. Khaykin, A. Hauchecorne, N. Mzé, and P. Keckhut. Seasonal variation of gravity wave activity at midlatitudes from 7 years of cosmic gps and rayleigh lidar temperature observations. *Geophysical Research Letters*, 42(4):1251–1258, 2015.

[4] Ulla Wandiger. *Lidar: Range-Resolved Optical Remote Sensing of the Atmosphere*, volume 102 of *Springer Series in Optical Sciences*, page 241-271. Springer New York, New York, NY, 2005.

[5] J Klett. Stable analytical inversion solution for processing lidar returns. *Applied Optics*, 20(2):211–220, 1981.

[6] U. von Zahn, G. von Cossart, J. Fiedler, K. H. Fricke, G. Nelke, G. Baumgarten, D. Rees, A. Hauchecorne, and K. Adolfsen.

The alomar rayleigh/mie/raman lidar: objectives, configuration, and performance. *Annales Geophysicae*, 18(7):815–833, 2000.

[7] P. A. Franken, A. E. Hill, C. W. Peters, and G. Weinreich. Generation of optical harmonics. *Phys. Rev. Lett.*, 7:118–119, Aug 1961.

[8] Bernd Mielke. Analog + photon counting. *Licel manual*, 02 2019.

[9] Adolf Smekal. Zur quantentheorie der dispersion. *Naturwissenschaften*, 11(43):873–875, 1923.

[10] K.S. Krishnan. The raman effect in crystals. *Nature*, 122(3074):477–478, 9 1929. An optional note.

[11] K. S. Krishnan. Influence of temperature on the raman effect. *Nature*, 122(3078):650, 1928.

[12] John Cooney. Measurement of atmospheric temperature profiles by raman backscatter. *Journal of Applied Meteorology*, 11(1):108–112, 1972.

[13] G. Herzberg. *Spectra of diatomic molecules*. Molecular spectra and molecular structure. Van Nostrand, 1950.

[14] G. Placzek and E. Teller. Die rotationsstruktur der ramanbanden mehratomiger moleküle. *Zeitschrift für Physik*, 81(3):209–258, Mar 1933.

[15] Andreas Behrendt. *Lidar: Range-Resolved Optical Remote Sensing of the Atmosphere*, volume 102 of *Springer Series in Optical Sciences*, page 272-305. Springer New York, New York, NY, 2005.

[16] C. M. Penney, R. L. St. Peters, and M. Lapp. Absolute rotational raman cross sections for n2, o2, and co2. *J. Opt. Soc. Am.*, 64(5):712–716, May 1974.

[17] J. Bendtsen and Finn Rasmussen. High-resolution incoherent fourier transform raman spectrum of the fundamental band of 14n2. *Journal of Raman spectroscopy*, 31(5):433–438, 6 2000. An optional note.

[18] M. Buldakov, I. Matrosov, and T. Popova. Determination of the anisotropy of the polarizability tensor of the o2 and n2 molecules. *Optics and Spectroscopy - OPT SPECTROSC*, 46:488–489, 01 1979.

[19] R.J Butcher, D. V. Willetts, and W. J. Jones. On the use of a fabry—perot etalon for the determination of rotational constants of simple molecules—the pure rotational raman spectra of oxygen and nitrogen. *The Royal Society*, 324(1557), 1971.

[20] D. Nedeljkovic, A. Hauchecorne, and M. . Chanin. Rotational raman lidar to measure the atmospheric temperature from the ground to 30 km. *IEEE Transactions on Geoscience and Remote Sensing*, 31(1):90–101, Jan 1993.

[21] U. Zahn, G. Cossart, J. Fiedler, K. Fricke, G. Nelke, G. Baumgarten, D. Rees, A. Hauchecorne, and K. Adolfsen. The alomar rayleigh/mie/raman lidar: objectives, configuration, and performance. *Annales Geophysicae*, 18(7):815–833, 2000.

[22] Kamil Stelmaszczyk, Marcella Dell'Aglio, Stanislaw Chudzyński, Tadeusz Stacewicz, and Ludger Wöste. Analytical function for lidar geometrical compression form-factor calculations. *Appl. Opt.*, 44(7):1323–1331, Mar 2005.

[23] Ulla Wandinger and Albert Ansmann. Experimental determination of the lidar overlap profile with raman lidar. *Appl. Opt.*, 41(3):511–514, Jan 2002.

[24] A. Berk, L.S. Bernstein, and D.C Robertson. Modtran: A moderate resolution model for lowtran 7. Technical report, Spectral Sciences, Inc, 99 South Bedford Street, Burlington, 4 1989.

[25] F.X. Kneizys, G.P. Anderson, E.P. Shettle, W.O. Gallery, L.W. Abreu, J.E.A. Selby, J.H. Chetwynd, and S.A. Clough. Users guide to lowtran 7. Technical report, Optical/Infrared technology division, AIR FORCE GEOPHYSICS LABORATORY, 8 1988.